Earth and Space Science

RESEARCH ARTICLE
10.1029/2021EA001935

Improving the Usability of Galileo and Voyager Images of Jupiter's Moon Europa

Michael T. Bland[1], Lynn A. Weller[1], Brent A. Archinal[1], Ethan Smith[1], and Benjamin H. Wheeler[1]

[1]Astrogeology Science Center, U. S. Geological Survey, Flagstaff, AZ, USA

Abstract NASA's Voyager 1, Voyager 2, and Galileo spacecraft acquired hundreds of images of Jupiter's moon Europa. These images provide the only moderate- to high-resolution views of the moon's surface and are therefore a critical resource for scientific analysis and future mission planning. Unfortunately, uncertain knowledge of the spacecraft's position and pointing during image acquisition resulted in significant errors in the location of the images on the surface. The result is that adjacent images are poorly aligned, with some images displaced by more than 100 km from their correct location. These errors severely degrade the usability of the Voyager and Galileo imaging data sets. To improve the usability of these data sets, we used the U.S. Geological Survey Integrated Software for Imagers and Spectrometers to build a nearly global image tie-point network with more than 50,000 tie points and 135,000 image measurements on 481 Galileo and 221 Voyager images. A global least-squares bundle adjustment of our final Europa tie-point network calculated latitude, longitude, and radius values for each point by minimizing residuals globally, and resulted in root mean square (RMS) uncertainties of 246.6 m, 307.0 m, and 70.5 m in latitude, longitude, and radius, respectively. The total RMS uncertainty was 0.32 pixels. This work enables direct use of nearly the entire Galileo and Voyager image data sets for Europa. We are providing the community with updated NASA Navigation and Ancillary Information Facility Spacecraft, Planet, Instrument, C-matrix (pointing), and Events kernels, mosaics of Galileo images acquired during each observation sequence, and individual processed and projected level 2 images.

Plain Language Summary Europa's subsurface ocean contains all the ingredients necessary for life, and this Jovian moon is therefore the target of continued scientific investigations and future exploration. Most of the pictures we have of Europa's surface were returned by the Voyager 1, Voyager 2, and Galileo spacecraft. These pictures provide insight into Europa's complex surface geology and ultimately clues to conditions within the ocean itself. Unfortunately, the pictures are hard to use because the location of the images on the surface are often incorrect. The result is that pictures that should overlap each other do not, or two apparently overlapping pictures show completely different scenes. In this work, we correct the locations of almost all the Galileo images and many of the Voyager images by identifying thousands of features that are in common between two or more images, and then mathematically calculating new locations for each feature such that the mismatch between pictures is globally minimized. We then created a set of mosaics that combine all the pictures taken during each Galileo flyby. We provide these mosaics, individual pictures, and improved camera pointing information to the community.

†Formerly.

Key Points:

- We improved the usability of 481 Galileo and 221 Voyager images of Europa by updating image locations on the surface
- Nearly the entire Europa Galileo image set is now "analysis-ready," requiring no additional image processing
- We have publicly released Galileo observation sequence mosaics, individual projected images, and updated camera pointing kernels

Supporting Information:

Supporting Information may be found in the online version of this article.

Correspondence to:

M. T. Bland,
mbland@usgs.gov

Citation:

Bland, M. T., Weller, L. A., Archinal, B. A., Smith, E., & Wheeler, B. H. (2021). Improving the usability of Galileo and Voyager images of Jupiter's moon Europa. *Earth and Space Science*, *8*, e2021EA001935. https://doi.org/10.1029/2021EA001935

Received 29 JUL 2021
Accepted 14 OCT 2021

Author Contributions:

Conceptualization: Michael T. Bland
Data curation: Michael T. Bland, Lynn A. Weller
Formal analysis: Michael T. Bland, Lynn A. Weller
Funding acquisition: Michael T. Bland
Investigation: Lynn A. Weller, Ethan Smith

1. Motivation

1.1. The Importance of Rigorous Control

For a planetary imaging data set to be of maximum use to the science community, the absolute and relative location of the images on the surface of a planet must be known with high accuracy and precision. For some planetary missions in which images are acquired from orbit, image locations derived from reconstructed Spacecraft, Planet, Instrument, C-matrix (pointing), and Events (SPICE) kernels (Acton et al., 2017) are sufficient for many scientific applications (e.g., morphologic analysis). However, the spatial accuracy of such reconstructed data is insufficient for investigating change detection, planning surface mission operation (e.g., rover traverse), or deriving higher-order data products (e.g., digital terrain models, DTMs). For missions in which data are acquired by multiple fast flybys of distant objects (e.g., many missions to the outer Solar System), uncertainties in the spacecraft and body locations and orientations are large enough to result

Methodology: Lynn A. Weller, Brent A. Archinal
Project Administration: Michael T. Bland
Supervision: Michael T. Bland
Visualization: Lynn A. Weller, Benjamin H. Wheeler
Writing – original draft: Michael T. Bland, Lynn A. Weller, Benjamin H. Wheeler
Writing – review & editing: Brent A. Archinal

in image location errors that render the images effectively unusable without additional data processing. In both cases, image locations can be improved through the use of photogrammetric techniques that update the location of images relative to each other. The images can then be tied to a previously existing reference frame (including a photogrammetric network) by fixing or constraining various solution parameters such as body orientation or the known locations of surface features, and the new solution can then serve as a new geodetic reference frame, useful for determining the location of features in the involved images. The resulting spatially "controlled" image data set can also then be used to generate mission-critical data products such as DTMs and orthoimages or orthomosaics, projected either onto simple body shape models (e.g., a sphere, rotational ellipsoid, or triaxial ellipsoid) or the DTMs.

Image data of Jupiter's moon Europa is a notable example of the second case described above. Images of Europa were acquired by the Voyager 1 and 2 (Smith, Soderblom, Beebe, et al., 1979; Smith, Soderblom, Johnson, et al., 1979), Galileo (Belton et al., 1996), New Horizons (Grundy et al., 2007), and Cassini spacecraft; however, the Galileo mission provides the only moderate- and high-resolution images (i.e., pixel-scales of <1 km/pixel) of Europa's surface. Unfortunately, the spacecraft position and orientation knowledge (encapsulated in the SPICE kernels) during image acquisition was uncertain, with the result that overlapping images acquired by different spacecraft, or even the same spacecraft on different flybys (for Galileo) are, in many cases, inaccurate by up to 100 km (Figure 1). This results in significant degradation of the usability of the data set. In order to use the data, investigators must choose to (a) use a single image for their analysis and disregard larger-scale context, (b) use multiple images, but disregard the spatial relationships between images (e.g., Dameron & Burr, 2018), (c) use an existing mosaic that has had image locations improved, but sacrifices image resolution (mosaics require that images are projected to a consistent pixel scale), or (d) perform photogrammetric control themselves, which requires significant time and understanding of photogrammetric techniques. Each of these choices has significant consequences for the quality of the resulting scientific analysis. The uncertainty in image locations also makes the production of higher-order data products challenging, as the relative orientation of stereo pairs must be corrected before they can be used for, for example, DTM generation (Bland, Galuszka et al., 2018). Given these challenges, improving the location of Europa images is essential to maximize the utility of this critical data set.

Improved image locations are also necessary for the development of a robust planetary spatial data infrastructure (PSDI) for Europa (Archinal et al., 2017; Laura et al., 2018). A PSDI is a collection of users, standards, policies, data, and data access mechanisms that maximize the utility and interoperability of spatial data sets acquired for a planetary body (Laura et al., 2017, 2018). Critical to a PSDI is the creation of "foundational" data products, which include geodetic coordinate reference frames, elevation, and orthoimages. Laura et al. (2018) list (their Table 2) foundational data products for Europa, such as the existing USGS Galileo-Voyager image mosaic, and provide information about each product, such as the varying levels of spatial resolution, spatial accuracy, and completeness. Subsequently, Laura and Beyer (2021) suggested a much more restrictive definition of what constitutes "foundational" data, arguing that image mosaics are not inherently foundational data products. In the Laura and Beyer (2021) conception, an image mosaic is only considered foundational if the images are relatively controlled (photogrammetrically image to image), rigorously tied to an existing geodetic coordinate reference frame at multiple points (i.e., absolutely controlled to a reference frame proxy such as Mars Orbiter Laser Altimeter data, or MOLA, for Mars), and rectified to an elevation model that removes topography-induced distortion. The Mars Digital Image Model 2.1 (MDIM2.1) (Archinal et al., 2003), which meets these criteria, is an archetypal foundational image mosaic. By their definition, the generation of a "foundational" mosaic for Europa is currently not possible. Although previously generated control networks and/or image mosaics (e.g., Becker et al., 2001) could be used as a proxy for the global coordinate reference frame, these earlier networks are not absolutely controlled to a MOLA-equivalent and have lower spatial accuracy than our current work. Additionally, existing data does not support the creation of a global elevation data set with which to perform high-fidelity rectification. However, we argue that although it is desirable to tie any image mosaic to an existing reference coordinate system and frame with many known ground points (e.g., from robotic or human occupation) or with extensive altimetric data, a photogrammetric control network also consists of a set of image tie points (identified ground features) with a set of derived coordinates and their relative precision. By defining an orientation model and the longitude of one of the points, a standard reference coordinate frame is established that allows for the position of any feature to be determined in an absolute sense at a known level of

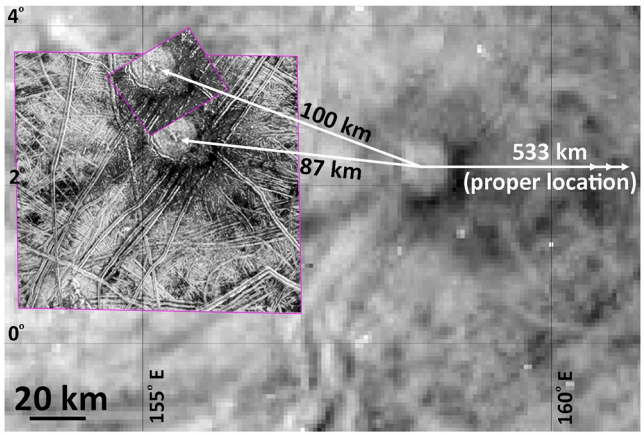

Figure 1. Example of poor image locations from reconstructed (default) pointing kernels (CKs). Each of the three images shows the 19 km crater Cilix, which defines Europa's longitude system, and are shown in equirectangular projection at the locations calculated from default kernels. White arrows are labeled with the offset distance between images. All three images are incorrectly located near 158°E (208°W), which is more than 500 km west of Cilix's IAU-defined longitude of 178°E (182°W), as indicated by the triple-headed arrow. The underlying low-resolution image is from Galileo observation 14ESGLOCOL01 at 1,450 m/pixel. The moderate resolution image is from Galileo observation 15ESCILIXS01 at 110 m/pixel. The highest resolution image is from Galileo observation 15ESCILIXS02 at 63 m/pixel.

horizontal and vertical accuracy. Here we have generated a photogrammetric control solution that provides for updated spacecraft pointing and tie point absolute latitude and longitude positions, with associated uncertainty information. It has been possible to place these positions in an absolute sense by fixing our solution to the International Astronomical Union or IAU-defined coordinate frame for Europa (including fixing the Europa orientation model and the longitude of the crater Cilix, shown in Figures 1 and 2), at the defined value of 182°W (178°E) (Archinal et al., 2018). Due to a lack of sufficient stereo coverage that would provide useful vertical information given the small variations in the radius of Europa's surface, the vertical position of the points has been fixed to the recommended spherical datum (the IAU-defined mean radius of 1,560.8 km [ibid.]). In turn, mosaic products have been generated using the control solution and these same IAU models, including the projection of the images onto the spherical datum. Improvements in these products or the superseding of them will only be possible with the acquisition of higher resolution images, and appropriate topographic information from stereo image coverage, altimetric information, or landed spacecraft with known coordinates. For now, for practical purposes, these products can serve as foundational data products, following earlier definitions such as those in Laura et al. (2018).

The need for improved image products and establishing a PSDI for Europa has been further necessitated by NASA's upcoming Europa Clipper mission. Europa Clipper's Europa Imaging System (EIS) camera will provide global decameter-scale image coverage, topographic mapping, color images, and local high-resolution (sub-meter pixel scale) images of Europa (Turtle et al., 2016). Europa Clipper's global image data set will be acquired by EIS during 40–50 individual flybys spread over the course of the multi-year mission (Turtle et al., 2016). Thus, images from Galileo and Voyager will be necessary to provide regional context until full coverage is acquired by the end of the mission. Although the EIS image data set will eventually supersede existing data sets for most purposes, existing data must be spatially accurate before Europa Clipper's arrival in the Jupiter system. Furthermore, planning of targeted, high-resolution EIS images may require accurate knowledge of feature locations from Galileo images if EIS context images cannot be acquired first. Searching for surface change between the Galileo and Europa Clipper missions is also enabled by accurate knowledge of Galileo image locations.

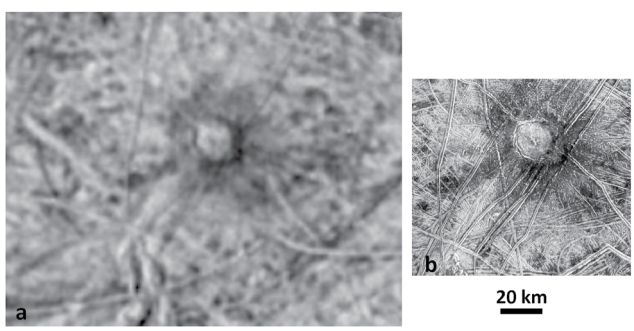

Figure 2. Comparison of (a) a portion of the existing U.S. Geological Survey basemap of Europa and (b) available, but uncontrolled, Galileo image data illustrating the loss of resolution when using the basemap alone. The basemap places Cilix in the correct location and provides geologic context but is low resolution (it uses the 1,450 m/pixel 14ESGLOCOL01 image downsampled to 500 m/pixel). Higher-resolution images exist but lack geologic context (as in b) and have incorrect location information (see Figure 1). The image in (b) is the 110 m/pixel image of Cilix from Galileo observation 15ESCILIXS01.

1.2. Previous Work

Several previous efforts have improved the locations of Europa images. Post-Voyager, the RAND Corporation, in association with the U.S. Geological Survey (USGS), created an image control network based on Voyager images alone (Davies & Katayama, 1981). Given the geometry of the Voyager 1 and 2 flybys, global coverage of Europa was not attainable (Batson et al., 1980; Davies & Katayama, 1981), so the resulting image products (and associated airbrush maps) are regional or hemispherical in coverage. After the Galileo mission, RAND and the USGS created a combined Voyager-Galileo control network, which was subsequently used to produce a global, relatively controlled, orthorectified (to a sphere) image basemap at 500 m per pixel (Becker et al., 2001; Davies et al., 1998) (https://astrogeology.usgs.gov/search/map/Europa/Voyager-Galileo/Europa_Voyager_GalileoSSI_global_mosaic_500m). This image base has been used extensively, including recently for global geologic mapping (Leonard et al., 2018). In an independent effort, a global color image basemap (also orthorectified to a sphere) was generated using updated image geometry by Paul Schenk at 200 m per pixel https://repository.hou.

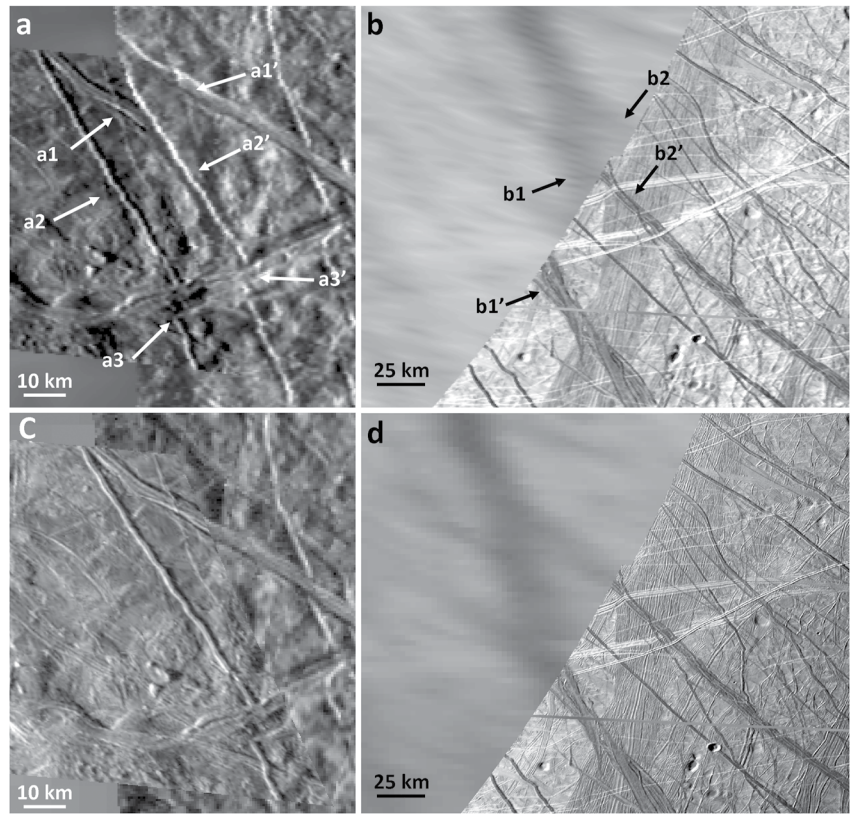

Figure 3. Examples of misregistrations in the existing U.S. Geological Survey basemap. In (a) the features marked a1, a2, a3 also appear at a1', a2', a3', respectively. In (b) the dark bands of Sarpedon Linea at b1 and b2 in the lower-resolution images are misaligned with the same dark bands at b1' and b2' in the adjacent higher-resolution image. Panels (c and d) show the same areas as in (a and b), respectively, but with proper image alignment after a bundle adjustment. Our thanks to Erin Leonard and Alex Patthoff for providing examples of misalignment.

usra.edu/handle/20.500.11753/1412. An unpublished controlled and orthorectified (to a sphere) near-global map was also created by Geoff Collins (see Laura et al. [2018] and Laura and Beyer [2021] for additional details). These latter products, since not clearly referenced (tied to) the earlier USGS/RAND products and their frames, constitute additional (unpublished) independent reference frames for Europa and (published) mosaics.

Although the products described above are generally high quality, they share several shortcomings. Perhaps most critically, the efforts to generate a "mosaic" or image "base" have led to control of only a subset of the available Europa images. Thus, many high-resolution images from Galileo have not had their locations improved because their small size renders them difficult to see in a global mosaic. Precisely because of their resolution, these images constitute some of the most important data returned from Galileo, yet they remain the hardest to use in a spatially consistent framework with other images. Even for the images included in the existing basemaps, updated SPICE kernels have not been produced from the associated control networks, meaning the improved location information cannot be applied to the raw images (The RAND solution does include updated image pointing information, but only in a RAND/ISIS2 specific format). This limitation is significant because image basemaps are intentionally generated with a consistent pixel scale. While appropriate when used as a map base for geologic mapping, the result is that higher resolution images appearing in the image base are shown at degraded resolution rather than their native resolutions (Figure 2). Additionally, some of the existing basemaps contain small misregistrations that result in both duplications of surface features (i.e., the same feature appearing twice) and misalignment of features (Figure 3). Finally, we note that the metadata associated with the existing image products is insufficient to understand the spatial accuracy of the data set. Determining the cases for which these data are "fit for use" is therefore difficult.

The new effort described here has improved upon these existing products and overcome many of the shortcomings described above. In the time since the original USGS image base was created, several improvements in photogrammetric techniques have become available to the planetary community. In particular, the use of automated, rather than manual methods for locating and measuring tie points, has allowed for a greatly increased number of points per image, and points measured on multiple overlapping images, compared to what was previously being measured manually. As described in Bland, Becker et al. (2018), including multiple images ("image measures") in a single tie point enables robust point localization, the determination of point location uncertainty, and the detection of outliers. Additionally, improvements in computational efficiency permit the use of nearly the entire Voyager and Galileo data set (see Section 2) and a relatively dense tie-point network. The result of these improvements is rigorous control of nearly the entire Galileo Europa image data set and much of the Voyager Europa data set, the assessment of image location accuracy, and the publication of updated locations that can be applied to raw data (i.e., freshly downloaded from the NASA Planetary Data System [PDS]). These efforts enable utilization (e.g., within a Geographic Information System, GIS, application) of an arbitrarily chosen set of Europa images with a consistent spatial reference frame that is tied to Europa's IAU-defined coordinate system.

1.3. Summary of the Current Work

Here we describe our efforts to improve the usability of the Europa data set. In Section 2, we describe our technical approach to photogrammetrically controlling Voyager and Galileo images, including a description of the positional uncertainty of the image set. Section 3 describes the products that are now available to the community, which include SPICE kernels, observation mosaics, and individual level 2 images. Section 4 describes how to obtain and use the data, and Section 5 summarizes the work.

2. Technical Approach

Below we first describe the Voyager and Galileo data sets used in this work (Section 2.1). We then describe our method for creating the global control network and performing the bundle adjustment to solve for the locations of tie points (Section 2.2). Finally, we describe how the images were tied to Europa's existing geodetic coordinate system (Section 2.3).

2.1. Data Sets

2.1.1. The Voyager Data

Launched in August (Voyager 2) and September (Voyager 1) of 1977, the two Voyager spacecraft flew through the Jupiter system in March (Voyager 1) and July (Voyager 2) of 1979. Each spacecraft carried an identically designed camera system, the Imaging Science Subsystem (ISS), consisting of both narrow- and wide-angle slow-scan vidicon cameras. The narrow-angle camera had a focal length of 1,500 mm, a 7.5 × 7.5-mrad field of view, and a 9.25-μrad angle subtended by each scan line. The wide-angle camera had a 200-mm focal length, 55.6 × 55.6-mrad field of view, and a 69.4-μrad angle subtended by each scan line. The actual focal lengths of each camera varied slightly (e.g., the prototype cameras had focal lengths of 1,499.125 mm and 201.568 mm for the narrow- and wide-angle camera, respectively) (Smith et al., 1977). We use the standard Voyager 1, Voyager 2, and Galileo camera models included in the USGS' ISIS software. Details of the Voyager ISS cameras and mission objectives can be found in Smith et al. (1977).

Each camera of the Voyager ISS used 800 scan lines per frame and 800 picture elements per line, resulting in images with 640,000 pixels per frame. The images include fiducial markers (reseaux) and corner markers used for making calibration measurements (e.g., focal length and camera distortion), and these markers must be removed before the images can be used for scientific applications, including control network development. Each camera also included its own eight-position filter wheel assembly, with a total of 12 unique filter combinations between the two cameras. The desire to image Europa in a variety of filters and the single Europa flyby of each Voyager mission resulted in the acquisition of numerous images with very similar viewing geometry.

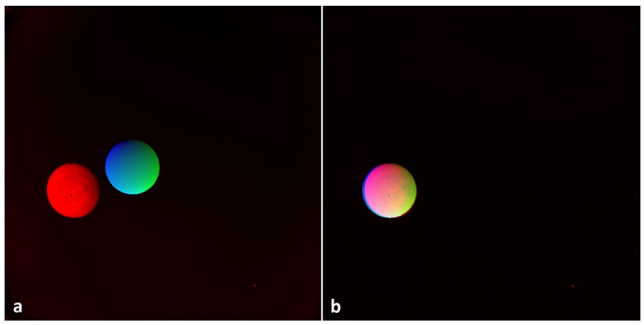

Figure 4. Illustration of "off body" Spacecraft, Planet, Instrument, C-matrix (pointing), and Events (SPICE) information from a Voyager 2 image of Europa. The red channel shows the location of Europa in the image space. The green and blue channels show the latitude and longitude backplane, respectively, as calculated directly from the SPICE information. In (a), the line/sample of image pixels on Europa are not associated with a latitude and longitude, making the image unusable. In (b) the SPICE (pointing information) has been corrected (using ISIS' *deltack* application as described in Section 2.1.1) to put the SPICE on the target.

We processed the raw Voyager images using the USGS' Integrated Software for Imagers and Spectrometers (ISIS 3.10) (http://doi.org/10.5281/zenodo.3697255, https://github.com/USGS-Astrogeology/ISIS3). We first ingested the images and applied SPICE (including the reconstructed CK and SPK, and the pck00010_msgr_v23.tpc PCK). Unfortunately, in most cases, the reconstructed Voyager SPICE is so poor that it lies completely off the body (Figure 4). For these cases, we resected the data by manually adjusting the CK using ISIS' *deltack* application. The *deltack* application requires that a user specifies that a specific line/sample in the image should have a particular latitude/longitude on the body. We use the "direct method" in which a rotation matrix is computed directly from the sample/line to the latitude/longitude from the surface intercept vectors from the spacecraft position. This approach requires two pieces of information: the line/sample of the center pixel of the body, and the latitude/longitude of the center according to the SPICE. We can then update the CK such that the center line/sample of the image aligns with the center latitude/longitude of the SPICE.

We calculated the center line/sample of the body using ISIS' *center* application, which calculates the "center of mass" of an image. We then calculate the central latitude/longitude of the SPICE (specifically we use the subspacecraft latitude and subspacecraft longitude) with ISIS' *campt* application, the latitude/longitude backplanes (which are calculated directly from the SPICE), and the *center* application. This approach is sufficient to adjust the SPICE to the target, which then enables us to subsequently control the data more rigorously using photogrammetric techniques (see Section 2.2). For the Voyager data set, we resected every image with a pixel scale <50 km/pixel. Some of these images were ultimately too poor (e.g., noisy) to resect and in a few cases the SPICE-derived target position lay completely outside the image and could therefore not be updated using this approach. Neither of these types of images were included in the photogrammetric control solution.

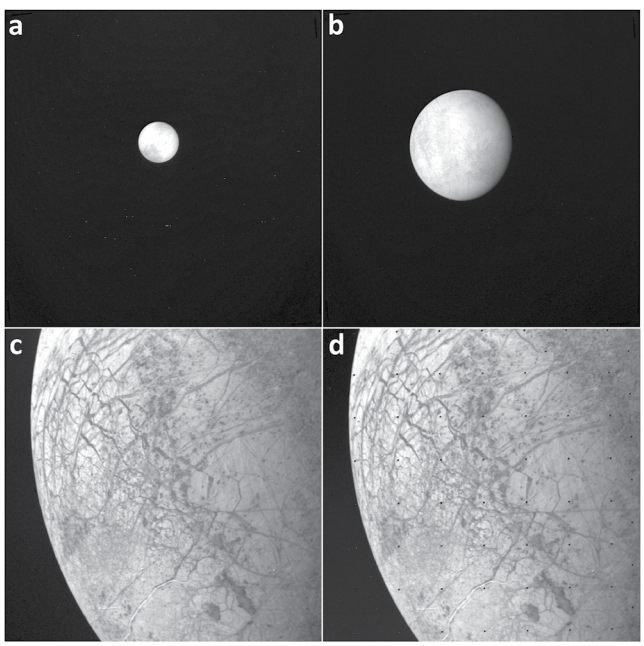

Figure 5. Examples of processed (a–c) and unprocessed (d) Voyager images at a variety of scales (mean value reported here). (a) Image c2058856 at 26.4 km/pixel. (b) Image c1633448 at 18.2 km/pixel. (c and d) Image c2064922 at 1.9 km/pixel, panel (c) shows the final processed image, whereas panel (d) shows the unprocessed image (note the black image reseaux). All three images were included in the Voyager control network.

With the images resected, we performed a modest amount of processing to aid image registration. Images were calibrated with the standard Voyager calibration (ISIS' *voycal*). After identification (ISIS' *findrx*), reseaux were removed (ISIS' *remrx*) and replaced by null pixels. The nulls were then "filled" using a series of low-pass filters applied to the null pixels alone. Finally, we trim three pixels off each edge of the image to provide a clean edge. Figure 5 shows an example of pre- and post-processed Voyager images at a variety of pixel scales.

Our final Voyager data set included 241 candidate images (as discussed in Section 2.2.1, not every image could be included in the control network) with pixel scales ranging from 1.63 km to 32.0 km. Figure 6 shows the distribution of the image pixel scales. Image coverage is nearly global; however, only a small fraction of the anti-Jovian hemisphere was imaged at scales of less than 2 km (Figure 7). The rest of Europa was imaged at pixel scales >10 km (excluding the poles, which were not imaged), although some regions only at large emission angles.

2.1.2. The Galileo Data

To follow up on the discoveries of the Voyager mission at Jupiter, the Galileo spacecraft was deployed from NASA's Space Shuttle Atlantis in October 1989, and, after gravity assist flybys of Venus and Earth (i.e., a VEEGA trajectory) and two asteroid encounters (Gaspra and Ida/Dactyl), entered Jupiter orbit in December of 1995. After orbit insertion (designated J0), Galileo's prime mission consisted of 11 orbits of Jupiter, each of which (except the fifth) targeted one of the Galilean satellites.

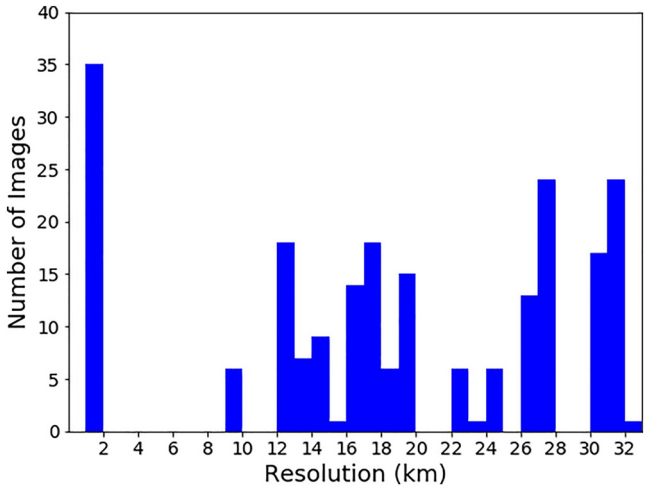

Figure 6. The distribution of pixel scales for Voyager images included in our control network.

Three of these orbits (E3, E4, E11) targeted Europa specifically; however, high-quality images were also acquired on untargeted flybys (see Alexander et al. [2009] for a summary). The "Galileo Europa Mission" (GEM) followed Galileo's prime mission with another 14 Jupiter orbits, of which the first eight (E12-E19) targeted Europa. Unfortunately, no data were obtained on E16 and E18 due to spacecraft safing events, and only gravity data were acquired on E13. Additional images of Europa were acquired during orbits E26, G28, and I33, which were part of the subsequent "Galileo Millennium Mission". Galileo's thirty-fourth orbit purposely put the spacecraft on a trajectory to collide with Jupiter in September of 2003.

The Galileo spacecraft was equipped with 10 instruments including the Solid-State Imager (SSI); a framing camera tasked with acquiring images with improved ground resolution and area coverage relative to Voyager. The optical system of the SSI was a modified flight spare of the 1,500-mm nominal focal length Voyager narrow angle camera, with an 8.1-mrad field of view, 10.16-µrad/pixel angular resolution, and 8 filter positions. Unlike the Voyager camera, the SSI used an 800×800-pixel charge-coupled device detector, which provided a substantial increase in sensitivity relative to Voyager's vidicon detector (Belton et al., 1992). During each flyby, images were acquired in one or more targeted sequences known as "observations". Each observation had a specific goal, for example, global imaging (usually over a single hemisphere or less), color imaging using multiple filters, or targeted imaging designed to capture a specific feature at smaller pixel scales. Observation sequences typically consist of 1–19 individual images, which were usually (though not always) acquired under similar illumination conditions and at a similar pixel scale.

The failure of Galileo's umbrella-like high-gain antenna to properly deploy after its second Earth flyby limited the data return from the mission. Despite this setback, the SSI acquired, and Galileo returned, more than 700 images of Europa. Not all of these images are of sufficient quality to be included in our work, either because the pixel scale is large (e.g., >20 km), they contained just a few lines of data, or they have extremely challenging geometry (e.g., navigation and eclipse images with no visible target). A total of 33 Galileo images were not included in this work. In order to work with the images, we first ingested them into ISIS, applied the standard radiometric calibration (ISIS' *gllssical*), applied a standard noise filter (radiation noise

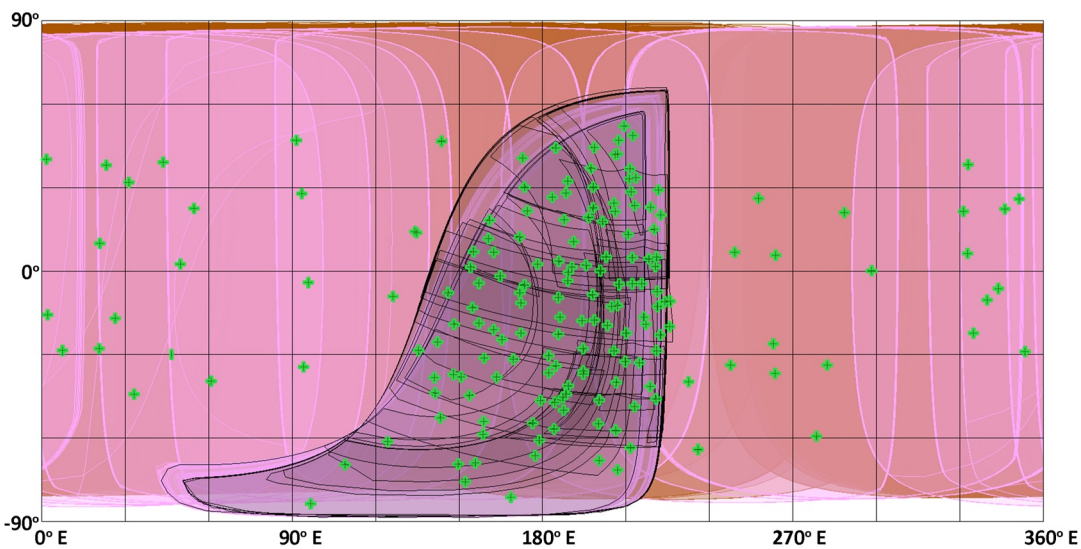

Figure 7. Voyager image footprints in equirectangular projection. The footprints outlined in black have a pixel scale <2 km/pixel. Pink footprints have a pixel scale between 9 and 20 km/pixel (no images have pixel a scale between 2 and 9 km/pixel), and the brown footprints in the background have a pixel scale >20 km/pixel. Green plus signs indicate the locations of tie points used in the Voyager-only network (see Section 2.2.1).

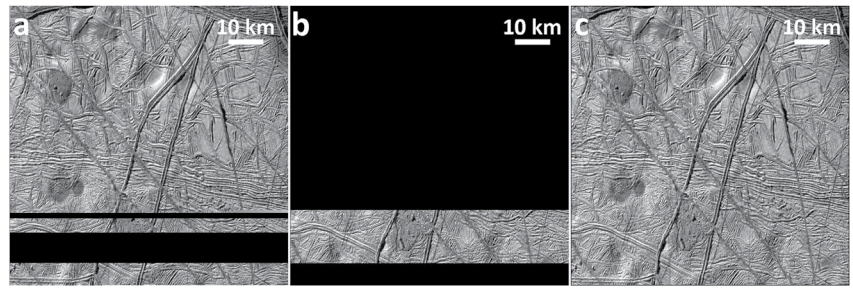

Figure 8. Example of reconstruction of "split" images. (a) Image s048488713 (located near Rhadamanthys Linea) is missing ~90 lines, which are contained in image s048488714 (b). The final image (c) is constructed by combining the two images by line/sample (using ISIS' *handmos* application).

is a challenge near Europa's orbit), and trimmed the images. Special handling was required for a handful of images that included incorrect PDS label information, or the necessity of resection due to SPICE being off the body (applicable only to full disk images), as described in Section 2.1.1.

In some cases, the image downlink was interrupted mid-transmission and had to be completed later, with the result that lines from a single frame are split into multiple image files. The complete image can be reconstructed by combining the multiple files into a single image by line/sample (using ISIS' *handmos* application, Figure 8). However, there are numerous cases in which portions of an image were never transmitted, and those images remain incomplete. Additionally, during image reconstruction choices must be made regarding the order in which the "pieces" of the images are placed. In general, we chose the least compressed portions of the images to sit on top of more compressed portions; however, some exceptions were made in cases where the more-compressed portion was clearly of higher data quality.

Our Galileo data set included 481 images with pixel scales ranging from 5.7 m/pixel to 19,500 m/pixel. Image coverage is nearly global over Europa; however, moderate-resolution images (500 m/pixel or better) are extremely limited in spatial extent (Figure 9).

2.2. Control Networks

In order to improve the locations of Galileo and Voyager images, we developed a global network of image tie points using ISIS. A *tie point* is a feature or pixel that can be identified and measured in two or more images whose locations on the planet's surface overlap. That is, they are correspondences between images. For a given tie point, we refer to each image in which the point can be identified as an image *measure*. Image measures are acquired either manually by a human operator or by automated means (or, quite often, a combination of the two). In general, assuming there are no sources of systematic error, the greater the number of image measures, n, included in a tie point, the better, by a factor of $1 / \sqrt{n}$, that the location of that point can be determined. The location of a point in three-dimensional space (e.g., latitude, longitude, radius) can be determined from just two measures, but in that case, the precision is unconstrained. With three or more measures, precision information can be obtained, and the statistical robustness of the location determination improves as the number of measures increases (see Bland, Becker et al. [2018] for details). The set of tie points and their measures is called a *control network*, and we refer to the *depth* of the network as a qualitative description of the number of image measures per tie point.

The control network is the input to the photogrammetric control process, in which a least-square bundle adjustment is performed (Brown, 1958). The bundle adjustment triangulates the ground coordinates (latitude, longitude, and radius) of each tie point and minimizes measure location residuals globally. The result is a mathematically robust improvement (or correction) of the entire global image data set simultaneously. We used ISIS' *jigsaw* application (Edmundson et al., 2012) to perform all of the bundle adjustments described here. We note that ISIS does not directly update the locations of images on the surface. Rather, the update is contained in the pointing and/or position of the camera when each image was acquired. The Voyager and Galileo images are from framing cameras, so solutions can be, and usually are, limited to spacecraft position and camera orientation. For line scan cameras, the spacecraft velocity and acceleration during image

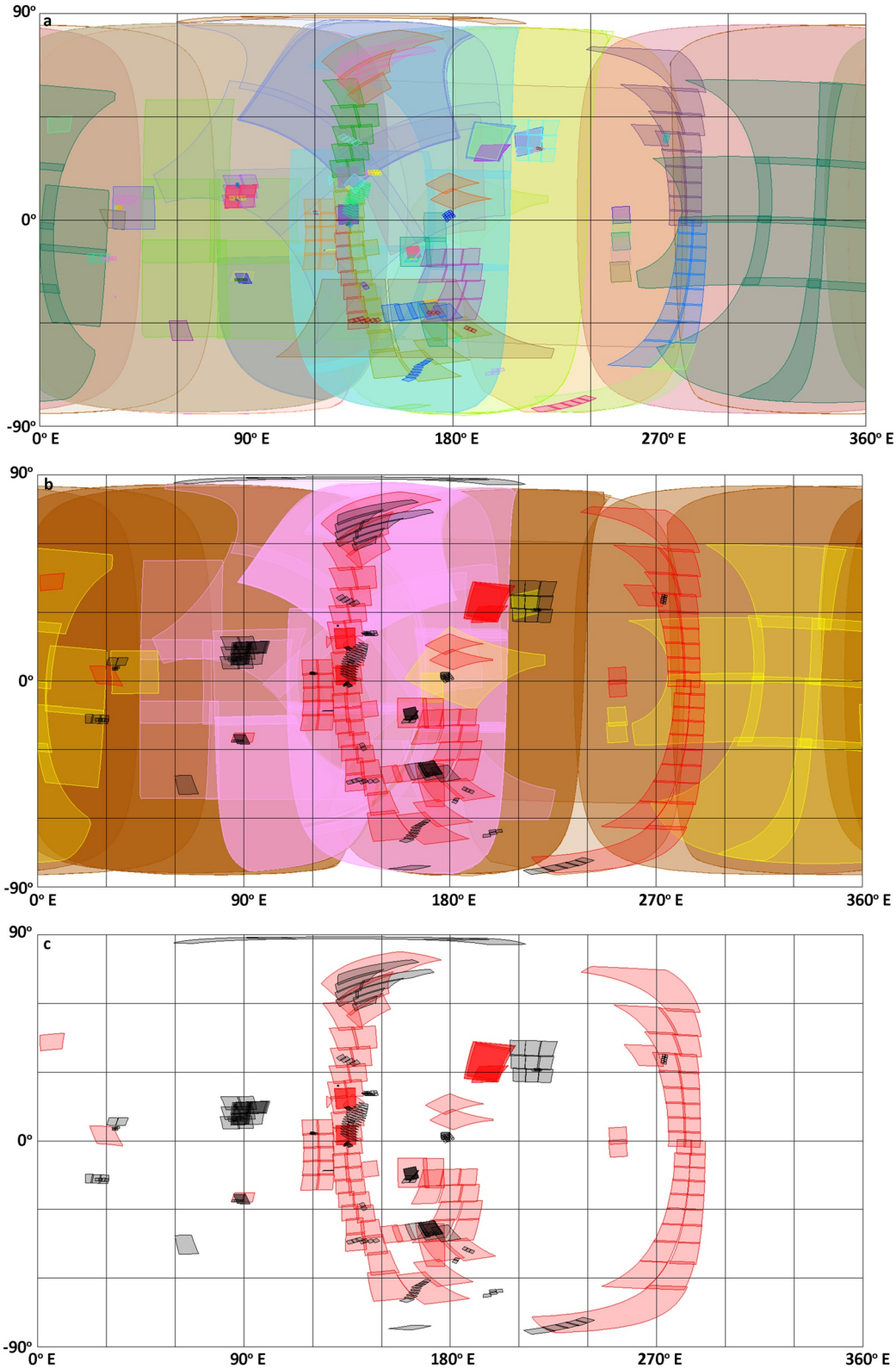

Figure 9. (a) Footprints in equirectangular projection of Galileo images of Europa included in this work illustrating image coverage. The footprints are color coded by Galileo observation sequence. (b) As in (a) except the footprints are color coded by image scale: >2,000 m/pixel (brown); 1,000–2,000 m/pixel (pink); 500–1,000 m/pixel (yellow); 200–500 m/pixel (red); <200 m/pixel (black). (c) As in (b), but only showing footprints for the highest-resolution images (<500 m/pixel, colors as in [b]).

Table 1
Summary of Control Network Statistics and Uncertainties

	Images	Points	Measures	RMS lat (m)	RMS lon (m)	RMS Rad (m)	Total RMS (pixels)
Voyager	221	178	4,790	2,102.8	1,866.5	179.1	0.52
Galileo	471	50,518	129,724	202.2	258.9	62.5	0.17
Bridge	50	322	644	1,972.3	1,889.5	93.3	0.17
Final	**697**	**51,336**	**135,782**	**246.6**	**307.1**	**70.5**	**0.32**

acquisition can also be determined. Here we do not solve for spacecraft position (SPICE SPK) because the narrow field of view of the Voyager and Galileo cameras results in a high correlation between spacecraft pointing and position parameters, and solving for both is redundant (and can result in singular solutions). Our photogrammetric control process, therefore, resulted in improved information about where the camera was pointing (NAIF SPICE pointing kernel [CK]) at the time images were acquired, which results in improved image locations after image-to-ground transformation.

In order to create a global control network for Europa that includes both Voyager (1 and 2) and Galileo images, we first generated three independent networks: a Voyager-only network, a Galileo-only network, and a "bridge" network that included key Voyager and Galileo images. Each of these networks was bundle adjusted separately to ensure a "clean" network (i.e., free from image misregistrations). The three clean networks were then merged into a single network and bundled together to update images' locations. Below we discuss each individual network before describing the results of our final network.

2.2.1. The Voyager Image Control Network

For the Voyager-only network we began with an existing control network that was originally developed by the RAND Corporation (Colvin, 1992) and subsequently converted to ISIS2 and then ISIS3 formats for use by the USGS. The network is available at https://astrogeology.usgs.gov/search/details/Europa/ControlNetworks/Europa_data. The network included 120 images from Voyager 1 and 2, 179 tie points, and 1,924 image measures. We ingested all 120 images, applied the resected SPICE kernels (see Section 2.1.1), calibrated the images, and performed a preliminary bundle adjustment of the control network. This bundle adjustment helped us identify tie points with high residuals (i.e., due to misregistrations of image measures), which could then be manually improved. The result was a refinement of the pre-existing RAND network.

The RAND network included only a subset of the Voyager 1 and 2 images that could potentially be controlled via our methodology. We, therefore, added 101 images (of the 121 initial candidates not already included in the existing network) to the network. Most of these added images were spatially redundant to the 120 images in the original network. To add these images, we attempted to automatically register each using an area-based maximum correlation algorithm with a goodness-of-fit threshold and weighted centroiding approach to subpixel registration. Unfortunately, the low resolution and highly variable illumination geometry rendered automated methods ineffective, and each point required manual intervention to determine whether the match was acceptable.

Our final Voyager-only control network, displayed in Figure 7, contains 221 Voyager 1 and 2 images, 178 tie points, and 4,790 measures. Note that the number of tie points in our final network is similar to that of the original RAND network; however, because we have roughly doubled the number of images, the depth of our network is greater. That is, we have increased the number of measures associated with each tie point, which can, in some circumstances, improve network quality. Bundle adjustment of the final network using a 500 m constraint on point radius and 2° constraint on camera angles resulted in root mean square (RMS) residuals of 2.1 km, 1.9 km, and 179 m in latitude, longitude, and radius, respectively, and a total RMS residual of 0.52 pixels. See summary data in Table 1.

2.2.2. The Galileo Image Control Network

For the Galileo-only network, we could find no previous network to use as a starting point. We, therefore, created the network "from scratch" by ingesting all Galileo images of Europa (i.e., everything with Target = Europa in the label), applying the reconstructed SPICE, calibrating the images, and performing a

simple noise filter. A few Galileo images required resection to improve the SPICE following the same procedure as applied to the Voyager images (Section 2.1.1). Galileo images that were downlinked in multiple files were reconstructed as described in Section 2.1.2.

Tie pointing of the Galileo images was performed using ISIS' *findfeatures* application, which uses the OpenCV (3.1) library of feature-based image matching algorithms. We performed two rounds of matching with different combinations of detector/extractor algorithms: SIFT/SIFT and FAST/BRIEF. The Scale Invariant Feature Transform (SIFT) algorithm (Lowe, 2004) is both a detector and extractor and is one of the oldest and most-tested feature-based matching algorithms. Although computationally slow, the resulting matches are generally correct with a high degree of confidence. The FAST/BRIEF pair utilizes a corner detector algorithm (FAST–Features from Accelerated Segment Test) (Rosten & Drummond, 2006) and an extremely efficient extractor (BRIEF–Binary Robust Independent Elementary Features) (Calonder et al., 2010) optimized for similar images (i.e., small differences in illumination, orientation, and scale). This pair is useful for increasing tie-point density between images within a single observation sequence. On their own, each algorithm pair had only limited success. However, taken together, the matches provided a global, relatively dense set of >1.4 million tie points. Unfortunately, most of the tie points contained only two image measures (i.e., pairwise matching). To increase the depth of the network, we used ISIS' *cnetcombinept* to combine points that were within 15 pixels of each other into a single point. The result was an acceptable decrease in tie-point density (to approximately 73,000 points), but an increase in the number of measures associated with each tie point (network depth). The network was further "thinned" to approximately 50,000 points using ISIS' *cnetthinner* application, which was used to set the maximum number of points per image to 500 (which is quite large for framing images).

Although tie-point matching with *findfeatures* produced a substantial number of matches (even after combining them as described above), it did not produce a fully connected global control network. Instead, the Galileo images were divided among ~30 separate "islands." All of the images in a given island were connected to each other but not to any other image in the data set. The largest island contained roughly 50% of the Galileo images. In contrast, many islands contained just one or two observation sequences, or even just a few images, that were well connected with each other (i.e., there are many tie points between them) but not to the rest of the data. Addressing the small islands first, we systematically (and manually) ensured that the images in each observation sequence were well connected, then refined and strengthened connections between the observation sequences within the island, and finally, created connections between different overlapping islands.

For the largest island, we first performed an independent bundle adjustment of the island in isolation and updated the relative location of images. This enabled us to perform another round of tie-point matching using *findfeatures* to find tie points where overlaps were previously too small, or not recognized at all, due to inaccurate reconstructed SPICE (the *fastgeom* option was used in *findfeatures* to reorient and rescale images using camera model and SPICE information before matching). We then manually connected the numerous small islands to the largest one (where they overlapped) and merged the networks to provide a global control network. A few Galileo observations were not included in the Galileo-only network but *are* included in the final network. This includes a set of images at Europa's north pole that can be tied to each other but do not overlap any other Galileo images and a Galileo observation that could not be tied to other Galileo data but could be tied directly to lower-resolution Voyager images.

The fully connected, global, Galileo-only control network includes 471 images, 50,518 tie points, and 129,724 image measures. We performed a bundle adjustment to solve for point latitude, longitude, and radius, and camera angles. We also allowed for camera twists. No a priori constraints were placed on latitude and longitude; however, a 500 m constraint was placed on point radius, and a 1° constraint was placed on camera angles. The resulting solution had RMS uncertainties of 202.2 m, 258.9 m, and 62.5 m in latitude, longitude, and radius, respectively, and a total RMS uncertainty of 0.17 pixels. See summary data in Table 1. Despite the relatively high accuracy, we note that the Galileo-only network barely closes in longitude. The Voyager images are necessary to provide robust longitudinal coverage.

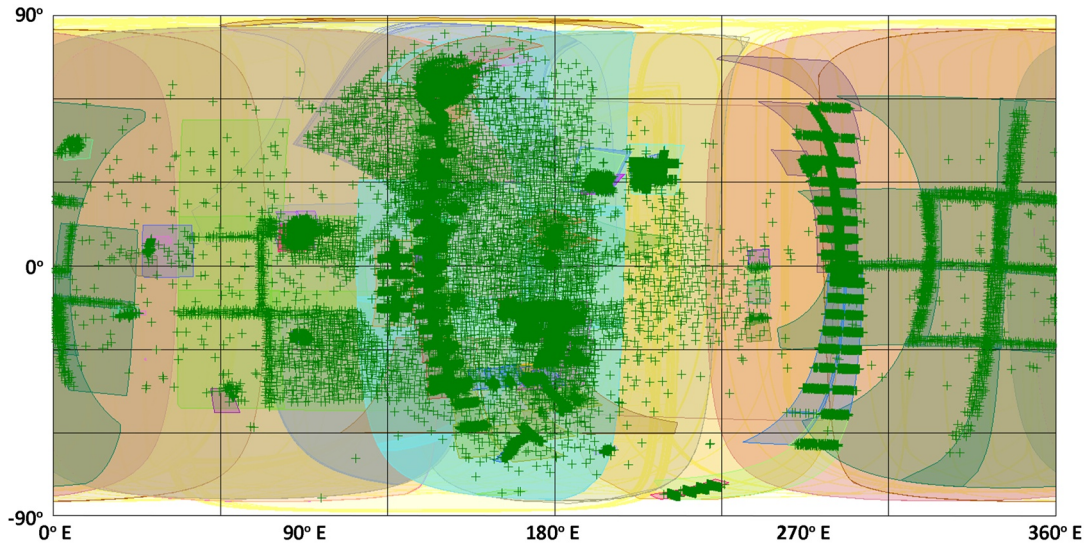

Figure 10. The final combined Galileo-Voyager control network (equirectangular projection). Image footprints are color-coded by observation as in Figure 9a, with the addition of yellow Voyager image footprints in the background. Green plus signs indicate the locations of tie points. Due to the sparsity of Voyager tie points, the distribution of points in this combined network appears nearly identical to that of the Galileo-only control network.

2.2.3. The Bridge Network

With the Voyager-only and Galileo-only networks completed, the next step was to bridge the two networks by finding a sufficient number of tie points between them. Since the Voyager data are much lower resolution than most of the Galileo data set, it was not feasible to match between every Galileo image and every Voyager image. Instead, we used a subset of each data set that had a similar pixel scale to one another and adequate overlap. Development of this "bridge network" was facilitated by a previously unreleased, combined Voyager-Galileo network archived internally at the USGS. The exact provenance of this network, which was converted to ISIS3 from an older format (effectively ISIS 1) is unclear. It apparently is *not* the network used to create the USGS Voyager-Galileo mosaics described in Section 1.2, as the image list differs substantially between the two. The preliminary network was manually refined to ensure that each tie point provided high-quality matches, and about a dozen points were manually added to key overlaps.

The final bridge network contains 50 Galileo and Voyager images, 322 tie points, and 644 measures. Note that the network consists of pairwise tie points. The majority of points in this network either connect two Galileo images (99 points) or two Voyager images (166 points). Only 67 points are connecting Galileo to Voyager, which is a result of the substantially different image scale and viewing geometry. The network is sparse but provides globally distributed tie points between Galileo and Voyager images that fully connect the Voyager-only and Galileo-only networks. Bundle adjustment of the bridge network alone resulted in a total RMS uncertainty of 0.17 pixels; however, due to the large spatial scale of the images, RMS uncertainty in latitude, longitude, and radius was 1.97 km, 1.89 km, and 93.3 m, respectively. See summary data in Table 1.

2.2.4. The Final Global Control Network

With the three separate control networks created, refined, and bundle adjusted, we merged the networks into a single combined network (using ISIS' *cnetmerge* application). The distribution of tie points in the final network is shown in Figure 10. We performed a single final bundle adjustment to update all image locations in which we solved for the latitude, longitude, and radius of each point, with a 500 m constraint on point radius and 1° constraint on camera angles. The final network had 697 images, 51,336 tie points, and 135,808 image measures. The total RMS uncertainty was 0.32 pixels, and the RMS uncertainty in latitude, longitude, and radius was 246.6, 307.0, and 70.5 m. See summary data in Table 1.

Note that the number of images, points, and measures in the final global network are not simply the sum of the Galileo-only and Voyager-only networks. As noted above, two Galileo observation sequences are included in the final network that could only be tied to Voyager images and were merged during this final

step. Those observation sequences include both "observation-only" tie points (i.e., points used to tie the individual images in an observation sequence to each other) and tie points that tie the entire Galileo observation to one or more Voyager images.

2.3. Adjustment to Europa's Prime Meridian

Europa's coordinate system is defined such that the crater Cilix is located at precisely 182°W longitude (178°E). For our initial bundle solution (i.e., Section 2.2.4) we included a tie point at Cilix's location and allowed it to adjust freely. Thus, during the final bundle solution, the location of Cilix adjusted slightly to a location of 181.968°W (178.032°E), a difference of 0.032°. Although small, such an offset is undesirable. In order to maintain Cilix at its IAU-defined longitude, we made a small adjustment to Europa's orientation (W_o) such that Cilix is located at precisely 182°W. The current IAU value of W_o (the ephemeris position of the Europa prime meridian at J2000.0 [Archinal et al., 2018]) is 36.022°. We, therefore, generated a new SPICE planetary constants kernel (PCK) with $W_o = 36.054°$ (36.022° + 0.032°). Performing a new bundle adjustment with these CK and PCK kernels confirms that Cilix ends up at 182°W (181.9991414°W). We then generated a final CK for every image. The result is a set of images with locations that are both improved relative to one another and constrained to the existing geodetic reference system for Europa.

We also solved for the direction of Europa's pole of rotation using our final control network and ISIS' *jigsaw* application (solved using our updated W_o and with the location of Cilix constrained). The resulting pole right ascension (RA) and declination (Dec) were 268.09° and 64.57°, respectively, at J2000.0. The values are consistent with current IAU values of 268.08° and 64.51°, respectively, at J2000.0. Although uncertainties are not explicitly indicated, Archinal et al. (2018) state that their tabulated expressions for the direction of the rotation pole are "generally accurate to one-tenth of a degree." We, therefore, do not recommend any changes to the IAU values based on our current work.

3. Released Data Products

3.1. Overview

The improved image locations calculated through bundle adjustment of our final combined Voyager and Galileo control network (Section 2) enable the creation of numerous products for use by the planetary community. We have chosen to provide the updated SPICE C-kernels (pointing), individual Galileo projected (level 2) images and the Galileo observation mosaics. These products provide a foundation from which users can easily generate their own, more-tailored products in ISIS or in a GIS. Below we describe each product.

3.2. SPICE C-Kernels

We generated new SPICE C-kernels (pointing) for 481 Galileo images, 58 Voyager 1 images, and 163 Voyager 2 images of Europa. The kernels let a user update the locations of individual, unprocessed PDS images, and are therefore best suited to those users who wish to process the original images themselves (e.g., calibration, noise removal, photometric correction), but would like to start with improved geometry and therefore image locations.

The kernels were generated from our final set of updated images (i.e., with the camera pointing improved through bundle adjustment of the final control network) using the ISIS application *ckwriter*. The kernels are discontinuous and indexed to the center of the exposure time. See https://naif.jpl.nasa.gov/pub/naif/toolkit_docs/C/req/ck.html for additional details. Because we have updated the ephemeris position of the Europa prime meridian at J2000.0 (W_o) to ensure that Cilix retains its correct position at 182°W (178°E) (Section 2.3) users must *also* use the new PCK when specifying the desired pointing kernel.

In Section 4 we provide instructions on how to apply the kernels to images within the ISIS environment. However, we emphasize that the kernels conform to NAIF requirements and can therefore be used by any software designed to work with NAIF SPICE information.

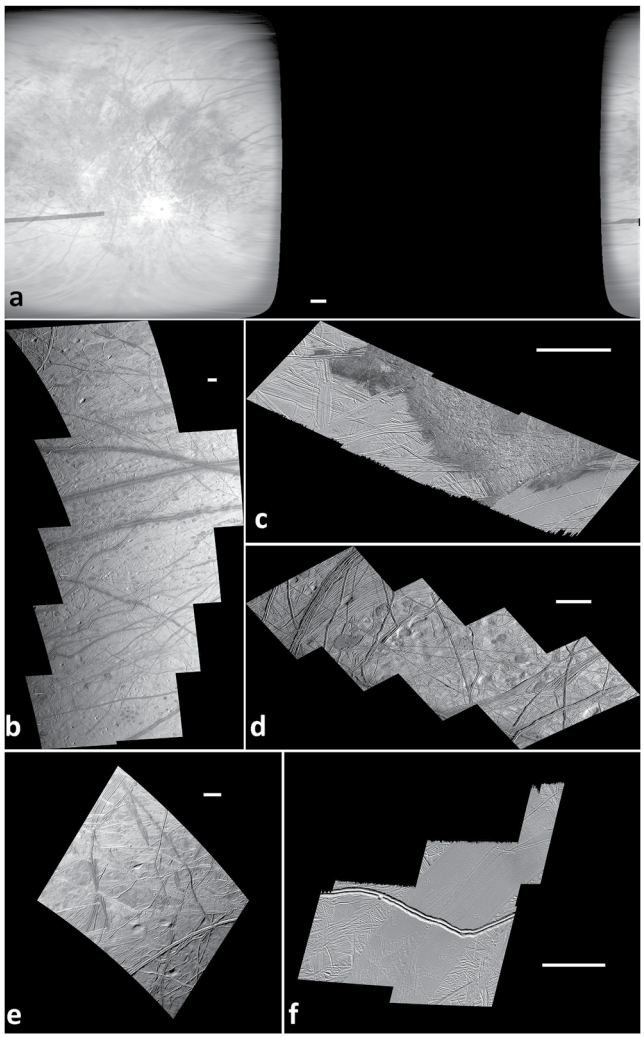

Figure 11. Examples of Galileo observation mosaics. The white scale bar in (a) is 200 km and is approximately correct at the equator. In all other panels, the scale bar is 20 km. (a) G2ESPHOTOM01, a global-scale mosaic of the trailing hemisphere. (b) 15ESREGMAP01, a regional-scale observation centered at 138°E (222°W), 40°N. (c) 17ESTHRACE01, a high-resolution observation of Thrace Macula. (d) 19ESRHADAM01, a high-resolution observation near Rhadamanthys Linea. Note that this observation lies within the regional observation shown in (b). See also Figure 13. (e) 15ESREGMAP01 in polar stereographic projection. Only the northernmost image is included. See panel (b). (f) 17ESTHYLIN01, high-resolution observation of Thynia Linea in south polar stereographic projection.

3.3. Observation Sequence Mosaics

As described in Section 2.1.2, during each flyby of Europa, the Galileo spacecraft acquired images in one or more targeted sequences known as "observations" (note that several Europa flybys did not acquire images). Because the images in an observation usually have similar illumination conditions and resolution, and often cover a discrete region of Europa, mosaics of the images within each observation provide a useful data set for investigations of Europa's surface. Each observation sequence is summarized in Table S1.

Using our updated level 2 (projected) images we created mosaics for each of Galileo's 92 observations that targeted Europa. The individual images have been calibrated and noise filtered as described in Section 2.1.2, but no photometric correction has been applied. Each image has been trimmed based on its photometric angles such that they do not extend beyond an incidence angle of 90° or an emission angle of 90°. However, 25 observations used lower, manually selected maximum incidence and/or emission angles between 90° and 80° to minimize image distortion. We choose to provide "average" mosaics, in which the pixel value in areas of image overlap is the average pixel values from each overlapping image. This provides smoother mosaics than traditional "on top" mosaics in which one image is placed on top of another. Mosaics are provided in equirectangular projection (also known as equidistant cylindrical, simple cylindrical, or Plate Carrée when the standard parallel is 0°) with latitude range −90°–90°. When individual images within an observation extend above 55° north or south latitude, we also provide a polar stereographic projection that extends from 55° N or S to the maximum absolute latitude. All projections assume that Europa is a sphere with a mean radius of 1,560.8 km (i.e., the IAU-defined mean radius; Archinal et al. [2018]). This projection is considered accurate because Europa's triaxial deviations from a sphere are small relative to the mean radius (~0.1%). Each image in a given observation is projected using the highest resolution (smallest pixel scale) found for the set of images in the observation. Using the highest resolution is acceptable because the images within a given observation generally differ by only a few tens of meters in pixel scale.

All mosaics are provided in a planetocentric east-positive, 0–360° longitude system for consistency with the current geologic map (Leonard et al., 2018) and the requirements of the Jupiter Icy moons Explorer and Clipper missions. An east-positive standard is also more readily used in GIS applications. However, because the IAU recommended system is planetographic, including west-positive 0–360° longitude (Archinal et al., 2018; Hall et al., 1971) we also provide west-positive labels for each mosaic. The latter system has also been used for all existing Voyager and Galileo data and mapping products, and most publications and databases related to Europa and is also required for use in archiving new products in the NASA Planetary Data System. Users can therefore choose whether they wish to use a planetocentric (east-positive longitudes) or planetographic (west-positive longitudes) coordinate system.

Figure 11 shows six examples of our Galileo observation mosaics that vary from global-scale imaging to regional mapping, to targeted imagining. The observation mosaics are the highest-order data products generated and are intended to be used easily within a GIS environment. When used as an entire data set, the 92 observation mosaics require less overhead than the 481 individual Galileo images (see Section 3.4). However, we expect that users are more likely to use just a few observation mosaics togeth-

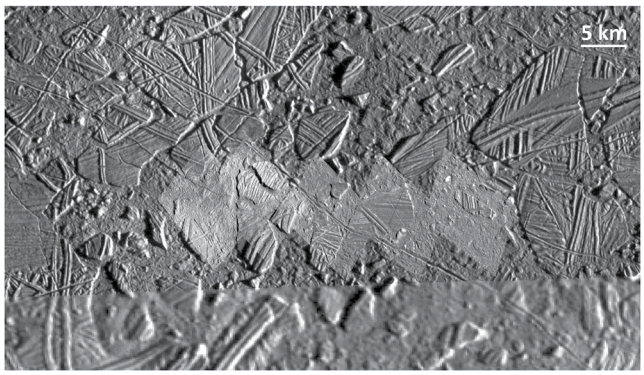

Figure 12. An example of how multiple observations mosaics can be used together. Here the target is Conamara Chaos. Shown is a screenshot from a GIS that includes three observation mosaics: a high-resolution mosaic (12ESCHAOS_01 at 9 m/pixel visible as light-toned images at figure center), a moderate-resolution mosaic (E6ESBRTPLN01 at 53 m/pixel visible as the background in the upper three-quarters of the figure), and a lower-resolution mosaic (E6ESDRKLIN01 at 179 m/pixel visible at the bottom quarter of the figure).

er; Figure 12 shows an example of such use. The image is a screenshot from a GIS in which we have simply downloaded and imported three observation mosaics that cover Conamara Chaos. The mosaics include a total of 15 images but require importing just three layers (one for each mosaic). Downloading the mosaics and importing them into a GIS only required a few minutes, saving hours of effort manually controlling the images. Figure 12 also illustrates the power of using observation mosaics at their native resolution. The five smallest pixel-scale images resolve small craters, fine tectonic fabrics, and surface textures not resolvable in the moderate-resolution mosaic, while the lower-resolution images provide geologic context. Toggling back and forth between the three layers (i.e., by turning layers on and off) gives the user a deeper understanding of the limits of the moderate- and low-resolution data, and allows extrapolation of textures observed at high-resolution to nearby areas seen only at lower resolution. The excellent registration of images in the figure also illustrates the high quality of the photogrammetric control. Figure 13, which shows two observation mosaics that include a portion of Rhadamanthys Linea further demonstrates these concepts.

3.4. Individual Projected Images

The generation of "average" observation mosaics obscures, to some extent, the original images that were used in the mosaic. We therefore also provide the 481 individual projected (level 2) Galileo images. These images were processed and projected as described in Section 3.3. Both photometrically trimmed and untrimmed versions are included, as are both equirectangular projections for all images and polar projections for images at >55° absolute latitude, resulting in a total of 1,104 images (450 equirectangular, 48 north polar projection, and 54 south polar projection in trimmed and untrimmed versions). The untrimmed versions include regions at high emission that are highly smeared due to the projection and heavily shadowed due to high incidence angles.

The individual projected images provide an intermediate product between the SPICE kernels (which require substantial additional image processing) and the observation mosaics described above. They are most suitable for users who want to use the data on an image-by-image basis, or who want to understand what each of the individual images that make up an observation look like. We show examples of level 2 images in Figure 14.

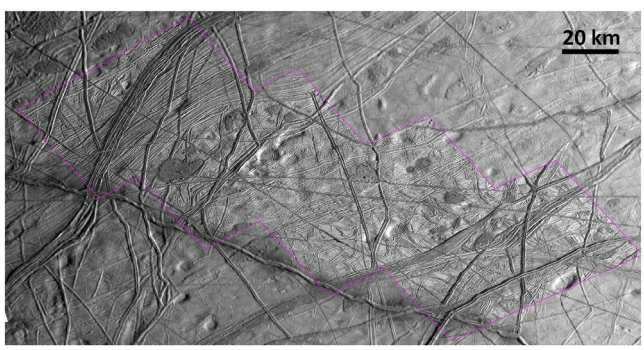

Figure 13. An example of how multiple observations mosaics can be used together. Here the target is Rhadamanthys Linea. Shown is a screenshot from a GIS that includes two observation mosaics: a high-resolution mosaic (19ESRHADAM01 at 63 m/pixel, visible at figure center), and a lower-resolution mosaic (15ESREGMAP01 at 228 m/pixel, visible as the background). A magenta outline has been added to aid the identification of the higher-resolution mosaic.

3.5. Solving for Europa's Shape

The determination of the latitude, longitude, and radius of each of the ~50,000 tie points in our network results in a point cloud from which we can derive Europa's shape. To solve for Europa's triaxial shape, we imported the point cloud (latitude, longitude, radius) into MATLAB and used its curve fitting toolbox to solve for the best-fitting ellipsoid. Specifically, we fit our data to the equation for a triaxial ellipsoid in terms of longitude (λ), co-latitude (θ, where $\theta = 90° - \phi$, and ϕ is the latitude), and radius (r).

$$r = \left[\frac{(\cos\lambda)^2 (\sin\theta)^2}{a^2} + \frac{(\sin\lambda)^2 (\cos\theta)^2}{b^2} + \frac{(\cos\theta)^2}{c^2} \right]^{\frac{-1}{2}},$$

where a, b, and c are the long (tidal) axis, intermediate axis, and short (polar) axis, respectively. We use a robust least-squares solution to fit the

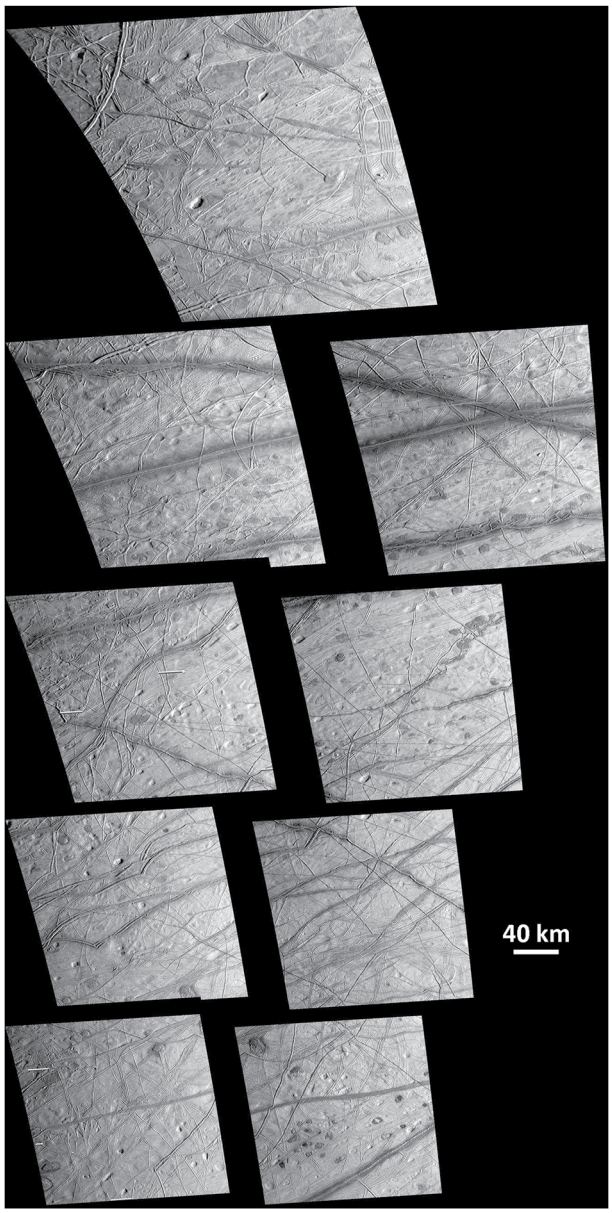

Figure 14. Example of individual projected (level 2) images. The nine images shown are from observation 15ESREGMAP01, as shown in Figures 11b. The images are centered at 138°E (222°W), 40°N.

Table 2
Europa's Shape and Orientation

Parameter	Current work	IAU value
a (km)	1562.598	1562.6
b (km)	1560.300	1560.3
c (km)	1559.496	1559.5
Pole RA	268.09°	268.08°
Pole Dec	64.57°	64.51°
W_o	36.054°	36.022°

data with a bisquare weighting method to reduce the influence of outliers. Using the point cloud derived from our nominal final *jigsaw* bundle solution, which included a 500 m constraint on the radius, we find *a*, *b*, and *c* axes of 1,562.598, 1,560.300, and 1,559.496 km, respectively, with an R^2 (the coefficient of determination) value of 0.9989. A summary is provided in Table 2. These values are effectively identical to the IAU values of 1,562.6, 1,560.3, and 1,559.5 km. Thus, our photogrammetric solution does not require, or even suggest, any modification of the current IAU recommended semi-axis values. A visualization of the solution is shown in Figure 15. We note that the imaging data are too sparse to solve for Europa's higher-order shape (Figure 15c) following the approach used for Enceladus as described in Bland et al. (2020).

To assess how our use of a constraint on the radius (nominally 500 m) during the bundle adjustment affected our shape solution we performed a sensitivity analysis in which we varied the bundle adjustment constraint on the radius (from 500 m to 10 km) and recalculated the shape. We find that, although the number and amplitude of outliers increased as weaker constraints were used, the resulting triaxial shape varied only slightly. For example, with a 10 km radius constraint during the bundle, the resulting semi-axes were 1,562.596, 1,560.313, and 1,559.498 km, respectively, with $R^2 = 0.8356$.

3.6. The Road Not Traveled

We have chosen not to generate a new global mosaic of Europa. Such mosaics already exist (e.g., the USGS mosaic described above), and generating a new "traditional" mosaic with a limited number of images projected to a consistent pixel scale would not provide a substantial improvement over these existing mosaics. The power of the products we provide is that *every* image can be used at its native resolution. Our work is therefore complementary to existing data products. The kernels we provide will also enable other users to easily update existing products (e.g., the color basemap generated by P. Schenk) or generate new, more-tailored products for specific purposes (e.g., regional or local basemaps at consistent scale for regional geologic mapping).

We have also chosen not to apply a photometric correction to the data set. When done rigorously, a photometric correction should preserve the integrity of the pixel values while removing the effects of viewing geometry. Although photometric models have been previously developed for Europa (Kirk et al., 2000; McEwen, 1991), recent work has shown that photometric behavior varies significantly with terrain type (Belgacem et al., 2020) and phase angle (i.e., the photometric parameters themselves are a function of phase [Dhingra et al., 2020]). These results are consistent with our previous experience, which found that applying globally derived photometric models resulted in sub-optimal corrections, especially for data at a high incidence of emission angles (much of our data) (Kirk et al., 2000). We, therefore, choose to preserve the calibrated I/F (intensity divided by solar flux) of each pixel in every image rather than apply an inadequate model to the data to produce an aesthetically pleasing mosaic. Again, the work described here will enable future improvements in modeling Europa's photometric properties to be easily applied to properly located images to generate a rigorously corrected mosaic if desired.

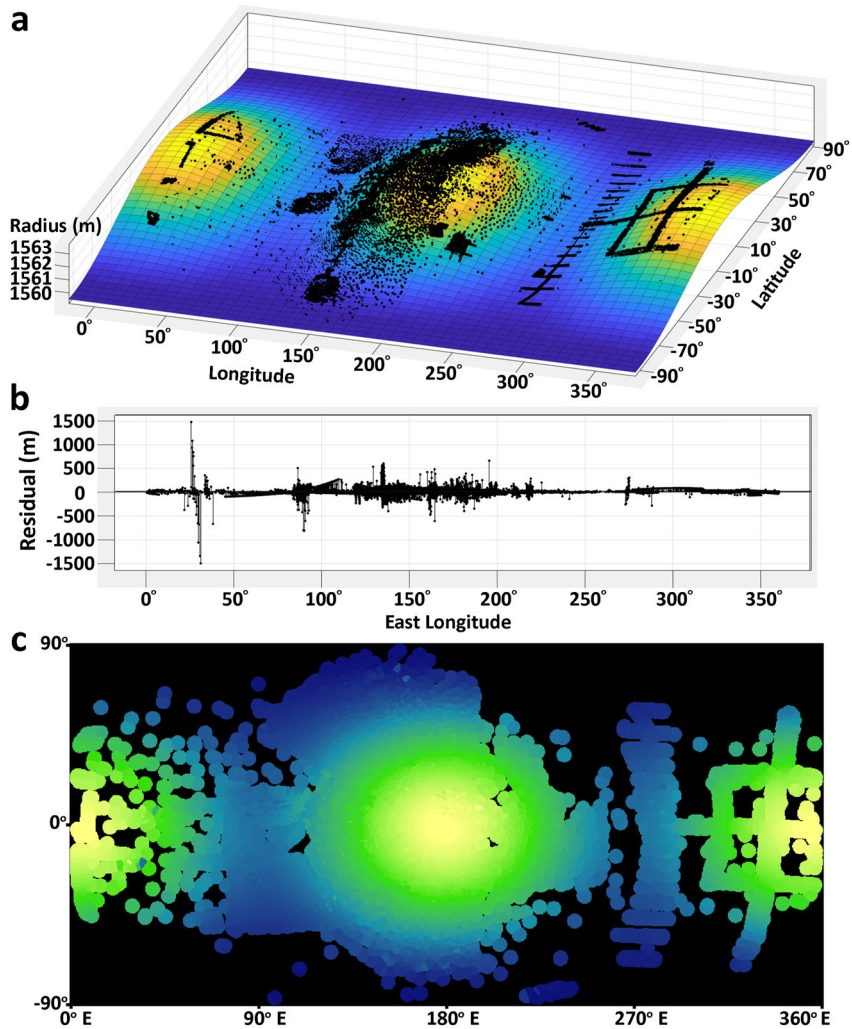

Figure 15. Visualization of Europa's shape determination. (a) The best fit triaxial ellipsoid (colors, yellow is high, blue is low) as determined by fitting to the latitude, longitude, and radius of the final network tie points (black dots). (b) The residuals (heights above the ellipsoid) from the best fit. Maximum residuals are 1.5 km; however, the vast majority of the fit residuals are less than 500 m. Panel a, and b, are output from MATLAB. (c) Visualization of Europa's triaxial shape determined by extrapolating the 3D point cloud to a digital terrain model (using the Ames Stereo Pipeline *point2dem* application). The triaxial shape is apparent, but shorter wavelength topography is not.

4. Data Access

The observation mosaics described above are currently available via the USGS' Astropedia data portal (https://doi.org/10.5066/P9VKKK7C). Due to the relatively small data volume, the mosaics are available for download as three zipped collections of GeoTIFF files: one for equirectangular projection, and one each in north and south polar projections. The collections include complete Federal Geographic Data Committee compliant metadata (https://www.fgdc.gov/metadata). These mosaics can simply be imported into a GIS for immediate use. The updated SPICE kernels are available from the same page (i.e., Astropedia). The kernels can be used manually within ISIS versions 3.9.0 and higher by explicitly specifying the kernel path for both the pointing and planetary constants kernel when running ISIS' *spiceinit* (i.e., set ck = galssi_eur_usgs2020.bc and pck = pck00010_msgr_v23_europa2020.tpc). The kernels are also released with ISIS versions 4.4.0 and higher and can be utilized simply by setting the 'cksmithed' parameter to TRUE when running the *spiceinit* application.

The individual level 2 images (and the mosaics) are available through a USGS-hosted SpatioTemporal Asset Catalog (STAC, https://stacspec.org/) (e.g., Vogt et al., 2019). The STAC permits both thumbnail browsing

and spatial search of the individual, projected images (both photometrically trimmed and untrimmed versions in equirectangular and polar projections, where appropriate), enabling the user to quickly access and download individual images for immediate use within a GIS or other application.

5. Summary

We have improved the usability of nearly the entire set of Galileo images, and many of the Voyager images, of Europa by improving their relative locations on the surface. To do so, we generated a photogrammetric control network containing more than 50,000 tie points and 135,000 image measures and performed a least-squares bundle adjustment to minimize tie point location residuals globally. Image locations uncertainty is 0.32 pixels (total RMS residual), and point location RMS uncertainties are approximately 247 m, 307 m, and 71 m, in latitude, longitude, and radius, respectively. The control network solution developed here is an improvement over the previous reference frame (e.g., as described in Becker et al. [2001]) and provides the current best geodetic coordinate reference frame for Europa. From this updated control network we have generated average mosaics for each Galileo observation sequence. These mosaics (equirectangular, and polar projection), the updated SPICE kernels (CK and PCK), and individual projected (level 2) images are publicly available through the USGS data portal, Astropedia, and a STAC. This work largely removes the image processing burden from the user, and enables, for example, investigators to simply import the image data into a GIS environment and begin analysis.

Data Availability Statement

The raw data used in this work is available in the NASA Planetary Data System Imaging Node at https://pds-imaging.jpl.nasa.gov/. All data products generated by this work are available from the U.S. Geological Survey Astropedia archive at https://doi.org/10.5066/P9VKKK7C and via a SpatioTemporal Asset Catalog browser at https://stac.astrogeology.usgs.gov/browser/#/ (navigate to "Jupiter Analysis Ready Data" folder).

Acknowledgments
This work benefited from control networks and software originally developed by Merton E. Davis, Tim R. Colvin, and Frank Y. Katayama of the RAND Corporation, from numerous conversations with Paul Schenk and Cynthia Phillips, and preliminary work by Tammy Becker, Moses Milazzo, and Glen Cushing. The authors thank Lauren Adoram-Kershner, Lillian Ostrach, Thomas Roatsch, and an anonymous reviewer for comments that greatly clarified the text and figures. This work was funded through an interagency agreement between NASA and the USGS. Any use of trade, firm, or product names is for descriptive purposes only and does not imply endorsement by the U.S. Government.

References

Acton, C., Bachman, N., Semenov, B., & Wright, E. (2017). A look toward the future in the handling of space science mission geometry. *Planetary and Space Science*, *150*, 9–12. https://doi.org/10.1016/j.pss.2017.02.013

Alexander, C., Carlson, R., Consolmagno, G., Greeley, R., & Morrison, D. (2009). The exploration history of Europa. In R. T. Pappalardo, W. B. McKinnon, & K. Khurana (Eds.), *Europa*. University of Arizona Press.

Archinal, B. A., Acton, C. H., A'Hearn, M. F., Conrad, A., Consolmagno, G. J., Duxbury, T., et al. (2018). Report of the IAU working group on cartographic coordinates and rotational elements: 2015. *Celestial Mechanics and Dynamical Astronomy*, *130*, 22. https://doi.org/10.1007/s10569-017-9805-5

Archinal, B. A., Kirk, R. L., Duxbury, T. C., Lee, E. M., Sucharski, R., & Cook, D. (2003). Mars Digital Image Model 2.1 control network. *Lunar and Planetary Science Conference*, *34*, 1485.

Archinal, B. A., Laura, J., Becker, T. L., Bland, M. T., & Kirk, R. L. (2017). *Foundational data products for Europa: A planetary spatial data infrastructure example*: American Geophysical Union Fall Meeting. Abstract #263468.

Batson, R. M., Bridges, P. M., Inge, J. L., Isbell, C., Masursky, H., Strobell, M. E., & Tyner, R. L. (1980). Mapping the Galilean Satellites of Jupiter with Voyager data. *Photogrammetric Engineering & Remote Sensing*, *46*, 1303–1312.

Becker, T., Archinal, B., Colvin, T., Davies, M., Gitlin, A., Kirk, R. L., & Weller, L. (2001). Final digital global maps of Ganymede, Europa, and Callisto. *Lunar and Planetary Science Conference*, *32*, 2009.

Belgacem, I., Schmidt, F., & Jonniaux, G. (2020). Regional study of Europa's photometry. *Icarus*, *338*, 113525. https://doi.org/10.1016/j.icarus.2019.113525

Belton, M. J. S., Head, J. W., Ingersoll, A. P., Greeley, R., McEwen, A. S., Klassen, K. P., et al. (1996). Galileo's first images of Jupiter and the Galilean Satellites. *Science*, *274*, 377–385. https://doi.org/10.1126/science.274.5286.377

Belton, M. J. S., Klaasen, K. P., Clary, M. C., Anderson, J. L., Anger, C. D., Carr, M. H., et al. (1992). The Galileo solid-state imaging experiment. *Space Science Reviews*, *60*, 413–455. https://doi.org/10.1007/BF00216864

Bland, M. T., Becker, T. L., Edmundson, K. L., Roatsch, T., Archinal, B. A., Takir, D., et al. (2018). A new Enceladus global control network, image mosaic, and updated pointing kernels from Cassini's 13-year mission. *Earth and Space Sciences*, *5*, 604–621. https://doi.org/10.1029/2018EA000399

Bland, M. T., Galuszka, D., Mayer, D. P., Beyer, R. A., Kirk, R. L., Schenk, P. M., & Fergason, R. L. (2018). How well do we know Europa's topography? Assessing variability in digital terrain models. *Lunar and Planetary Science Conference*, *49*, 2193.

Bland, M. T., Weller, L. A., Mayer, D. P., & Archinal, B. A. (2020). A global shape model for Saturn's moon Enceladus from a dense photogrammetric control network. *ISPRS Annals of the Photogrammetry, Remote Sensing and Spatial Information Sciences*, *V-3–2020*, 579–586. https://doi.org/10.5194/isprs-annals-V-3-2020-579-2020

Brown, D. C. (1958). *A solution to the general problem of multiple station analytical stereotriangulation*. RCA Data Reduction Technical. Report No. 43.

Calonder, M., Lepetit, V., Strecha, C., & Fua, P. (2010). Brief: Binary robust independent elementary features. In K. Daniilidis, P. Maragos, & N. Paragios (Eds.), *Computer vision – ECCV 2010. Eccv 2010. Lecture notes in computer science* (Vol. *6314*, pp. 778–792). Springer. https://doi.org/10.1007/978-3-642-15561-1_56

Colvin, T. R. (1992). *Photogrammetric algorithms and software for spacecraft optical imaging systems, A RAND Note*, N-3330-JPL. Retrieved from https://www.rand.org/pubs/notes/N3330.html

Dameron, A. C., & Burr, D. M. (2018). Europan double ridge morphometry as a test of formation models. *Icarus*, *305*, 225–249. https://doi.org/10.1016/j.icarus.2017.12.009

Davies, M. E., Colvin, T. R., Oberst, J., Zeitler, W., Schuster, P., Neukum, G., et al. (1998). The control networks of the Galilean satellites and implications for global shape. *Icarus*, *135*, 372–376. https://doi.org/10.1006/icar.1998.5982

Davies, M. E., & Katayama, F. Y. (1981). Coordinates of features on the Galilean satellites. *Journal of Geophysical Research*, *86*, 8635–8657. https://doi.org/10.1029/JA086iA10p08635

Dhingra, R. D., Buratti, B. J., & Seignovert, B. (2020). Europa Clipper preparatory photometry to constrain surface properties. *Lunar and Planetary Science Conference*, *51*, 2456.

Edmundson, K. L., Cook, D. A., Thomas, O. H., Archinal, B. A., & Kirk, R. L. (2012). Jigsaw: The ISIS3 bundle adjustment for extraterrestrial photogrammetry. *International Annals of Photogrammetry, Remote Sensing, and Spatial Information Sciences*, *I-4*, 203–208. https://doi.org/10.5194/isprsannals-i-4-203-2012

Grundy, W. M., Buratti, B. J., Cheng, A. F., Emery, J. P., Lunsford, A., McKinnon, W. B., et al. (2007). New Horizons mapping of Europa and Ganymede. *Science*, *318*, 234–237. https://doi.org/10.1126/science.1147623

Hall, J. S., Sagan, C., Middlehurst, B., Pettengill, G. H. (1971). Commission 16: Physical Study of Planets and Satellites, Report of Meetings: 20, 24, 25, and 26 August 1970, 128–137. In C. de Jager & A. Jappel (Eds.), *Proceedings of the Fourteenth general assembly Brighton 1970*, D. Reidel Publishing Company.

Kirk, R. L., Thompson, K. T., Becker, T. L., & Lee, E. M. (2000). Photometric modeling for planetary cartography. *Lunar and Planetary Science Conference*, *31*, 2025.

Laura, J. R., & Beyer, R. A. (2021). Knowledge inventory of foundational data products in planetary science. *The Planetary Science Journal*, *2*, 18. https://doi.org/10.3847/PSJ/abcb94

Laura, J. R., Bland, M. T., Fergason, R. L., Hare, T. M., & Archinal, B. A. (2018). Framework for the development of planetary spatial data infrastructure: A Europa case study. *Earth and Space Sciences*, *5*, 486–502. https://doi.org/10.1029/2018EA000411

Laura, J. R., Hare, T. M., Gaddis, L., Fergason, R. L., Skinner, J. A., Hagerty, J. J., & Archinal, B. A. (2017). Toward a planetary spatial data infrastructure. *ISPRS International Journal of Geo-Information*, *6*, 181. https://doi.org/10.3390/ijgi6060181

Leonard, E., Patthoff, A., Senske, D., & Collins, G. (2018). The Europa global geologic map. *Planetary Geologic Mappers Annual Meeting, 7008*.

Lowe, D. G. (2004). Distinctive image features from scale-invariant keypoints. *International Journal of Computer Vision*, *06*, 91–110. https://doi.org/10.1023/B:VISI.0000029664.99615.94

McEwen, A. S. (1991). Photometric functions for photoclinometry and other applications. *Icarus*, *92*, 298–311. https://doi.org/10.1016/0019-1035(91)90053-V

Rosten, E., & Drummond, T. (2006). Machine learning for high speed corner detection. In A. Leonardis, H. Bischof, & A. Pinz (Eds.), *Computer vision – ECCV 2006. Eccv 2006. Lecture notes in computer science* (Vol. *3951*, pp. 430–443). Springer. https://doi.org/10.1007/11744023_34

Smith, B. A., Briggs, G. A., Danielson, G. E., Cook, A. F., Davies, M. E., Hunt, G. E., et al. (1977). Voyager Imaging Experiment. *Space Science Reviews*, *21*, 103–127. https://doi.org/10.1007/BF00200847

Smith, B. A., Soderblom, L. A., Beebe, R., Boyce, J., Briggs, G., Carr, M., et al. (1979). The Galilean Satellites and Jupiter: Voyager 2 imaging science results. *Science*, *206*, 927–950. https://doi.org/10.1126/science.206.4421.927

Smith, B. A., Soderblom, L. A., Johnson, T. V., Ingersoll, A. P., Collins, S. A., Shoemaker, E. M., et al. (1979). The Jupiter system through the eyes of Voyager 1. *Science*, *204*, 951–972. https://doi.org/10.1126/science.204.4396.951

Turtle, E. P., McEwen, A. S., Collins, G. C., Fletcher, L., Hansen, C. J., Hayes, A. G., et al. (2016). The Europa Imaging System (EIS): High-resolution imaging and topography to investigate Europa's geology, ice shell, and potential for current activity. *Lunar and Planetary Science Conference*, *47*, 1626.

Vogt, A., Wytzisk-Arens, A., Drost, S., Jirka, S. (2019). Cloud based discovery and processing of geospatial data. In P. Kyriakidis, D. Hadjimitsis, D. Skarlatos, & A. Mansourian (Eds.), *Accepted Short Papers and Posters from the 22nd AGILE Conference on Geo-information science. Cyprus University of Technology 17–20 June 2019, Limassol, Cyprus. ISBN 978-90-816960-9-8*. Stichting AGILE.